Contents lists available at ScienceDirect

Science of the Total Environment

Extent of As(III) versus As(V) adsorption on iron (oxyhydr) oxides depends on the presence of vacancy cluster-like micropore sites: Insights into a seesaw effect

Juan Liu [a], Yixin Duan [a], Hao Chen [b], Bangjiao Ye [b], Hongjun Zhang [b,*], Wenfeng Tan [a], Andreas Kappler [c], Jingtao Hou [a,*]

[a] State Environmental Protection Key Laboratory of Soil Health and Green Remediation, Hubei Key Laboratory of Soil Environment and Pollution Remediation, College of Resources and Environment, Huazhong Agricultural University, Wuhan 430070, China
[b] State Key Laboratory of Particle Detection and Electronics, University of Science and Technology of China, Hefei 230026, China
[c] Geomicrobiology, Department of Geosciences, University of Tübingen, Tübingen 72076, Germany

HIGHLIGHTS

- Poorly-crystalline iron (oxyhydr)oxides form abundant cluster-like micropore sites
- Vacancy cluster-like micropores with 10–20 atom gaps provide extra As adsorbed sites
- Micropores are conducive for adsorbing smaller-sized As(III) than larger-sized As (V)
- Vacancy cluster-like micropores act as active "hotspot" affecting the fate of arsenic

GRAPHICAL ABSTRACT
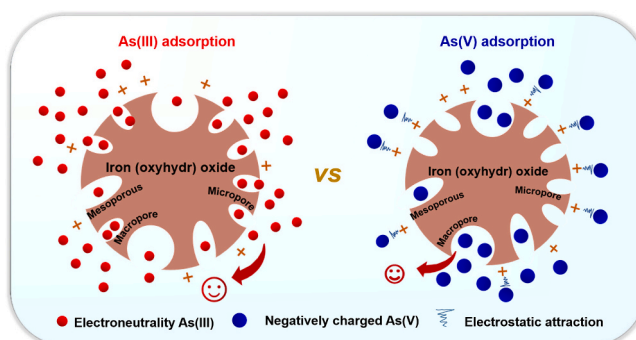
ARTICLE INFO

Editor: Baoliang Chen

ABSTRACT

Iron (oxyhydr)oxides are ubiquitous in terrestrial environments and play a crucial role in controling the fate of arsenic in sediments and groundwater. Although there is evidence that different iron (oxyhydr)oxides have different affinities towards As(III) and As(V), it is still unclear why As(V) adsorption on some iron (oxyhydr) oxides is larger than As(III) adsorption, while it is opposite for other ones. In this study, six typical iron (oxyhydr) oxides are selected to evaluate their adsorption capacities for As(III) and As(V). The characteristics of these iron minerals such as morphology, arsenic adsorption species, and pore size distribution are carefully examined using transmission electron microscopy (TEM), energy dispersive X-ray spectroscopy (EDS), positron annihilation lifetime (PAL) spectroscopy, and X-ray absorption spectroscopy (XAS). We confirm a seesaw effect occurred in different iron minerals for As(III) and As(V) immobilization, i.e., at pH 6.0, adsorption of As(V) on hematite (0.73 μmol m^{-2}) and magnetite (0.33 μmol m^{-2}) is higher than for As(III) (0.61 μmol m^{-2} and 0.27 μmol m^{-2}, respectively), for goethite and lepidocrocite it is almost equal, while As(III) sorption on ferrihydrite (5.77 μmol m^{-2}) and schwertmannite (28.41 μmol m^{-2}) showed higher sorption than As(V) (1.53 μmol m^{-2} and 12.99 μmol

* Corresponding authors.
E-mail addresses: hjzhang8@ustc.edu.cn (H. Zhang), houjt87@163.com (J. Hou).

m^{-2}, respectively). PAL analysis demonstrates that ferrihydrite and schwertmannite have a large concentration of vacancy cluster-like micropores, significantly more than goethite and lepidocrocite, followed by hematite and magnetite. The difference of adsorption of As(III) and As(V) to different iron (oxyhydr)oxides is due to differences in the abundance of vacancy cluster-like micropore sites, which are conducive for smaller size As(III) immobilization but not for larger size of As(V). The findings of this study provide novel insights into a seesaw effect for As(III) and As(V) immobilization on naturally occurring iron mineral.

1. Introduction

Iron (Fe) ranks fourth among all elements on Earth's surface and is widely distributed in soil, water, animals, and plants (Kim and Guerinot, 2007). Iron-bearing (oxyhydr)oxides are found in virtually all terrestrial and aquatic environments. Because of their high reactivities, large adsorption capacities as well as their ubiquitous existence, iron minerals widely affect nutrient cycling, heavy metal adsorption processes, organic carbon sequestration and turnover, and mineral redox transformation processes (Jubb et al., 2018; Liu et al., 2021; Ni et al., 2022; Pang et al., 2007; Wang et al., 2021). However, due to fluctuating environmental conditions (e.g., pH, temperature, redox conditions and other factors), a series of different iron (oxyhydr)oxides with different morphology and crystallinity is formed including poorly-crystalline iron (oxyhydr)oxides (e.g., ferrihydrite) and well-crystalline iron oxides (e. g., hematite). These iron (oxyhydr)oxides have different microstructural characteristics, giving them unique physico-chemical properties and thus greatly affecting the migration of contaminants, especially arsenic (As), a highly toxic and carcinogenic metalloid.

Iron minerals have been shown to influence the migration of arsenic due to their large adsorption affinities as well as their high abundance, thereby contributing to the arsenic sinks in paddy soil and groundwater. The release of arsenic from As-bearing iron (oxyhydr)oxides in the environment is an undesirable process that leads to an increase in its environmental risk. In general, arsenic is distributed in the environment mainly in the inorganic forms of arsenate [As(V)] and arsenite [As(III)], with As(III) commonly regarded as being more toxic and showing weaker adsorption affinity to iron (oxyhydr)oxides than As(V). For example, Giménez et al. observed that As(V) adsorption on naturally occurring magnetite and goethite was higher than that of As(III) (Giménez et al., 2007). In our previous work, we also found larger As(V) adsorption on laboratory-synthesized hematite relative to As(V) (Zheng et al., 2020). These results imply that oxidation of As(III) to As(V) leads to an increase in As(III) immobilization on iron (oxyhydr)oxides (Bujňáková et al., 2013; Giménez et al., 2007; Mandal and Suzuki, 2002; Raven et al., 1998). However, a growing body of literature confirmed that the adsorption affinity of As(III) on some poorly-crystalline iron (oxyhydr)oxides relative to As(V) is not as low as expected. For example, Zhang et al. evaluated As(III) and As(V) adsorption on poorly-crystalline ferrihydrite and found that the maximum As(III) adsorption amount was several times larger than that of As(V) (Zhang et al., 2014; Zhang et al., 2012). Qi and Pichler further observed that ferrihydrite exhibited higher adsorption of As(III) in comparison to As(V) within the pH range of 4–10. (Qi and Pichler, 2014). In principle, it is easy to understand that the discrepancy of As(III) and As(V) adsorption on different iron (oxyhydr)oxides arises from their different properties, such as morphology, specific surface area, and surface charge. However, the mechanisms governing the differential immobilization of As(III) and As(V) by various iron (oxyhydr)oxides remain poorly understood, as some materials show preferential adsorption towards As(III) while others exhibit higher affinity towards As(V). Due to the variety of iron (oxyhydr)oxides in nature, filling this knowledge gap is important to understand the migration and fate of arsenic controlled by different iron minerals.

Herein, six typical iron (oxyhydr)oxides with diverse crystallinities, including hematite, goethite, magnetite, lepidocrocite, ferrihydrite, and schwertmannite were conducted to evaluate their adsorption capacities for As(III) and As(V). The changes of microstructure, including

morphology, particle size, pore size distribution for these iron-bearing minerals reacting with As(III) or As(V) were carefully investigated. The chemical speciation and adsorption/desorption kinetics for As(III) and As(V) on six selected iron (oxyhydr)oxides were also examined. The purposes of this study are: (1) to evaluate the adsorption capacities of As (III) and As(V) on six typical iron (oxyhydr)oxides, (2) to evaluate the microstructural characteristics in the different iron minerals, and (3) to reveal the underlying mechanism of the differences in adsorption behavior of As(III) and As(V) on the iron minerals.

2. Materials and methods

2.1. Mineral preparation

Hematite and goethite were prepared by a coprecipitation approach following previous reports (Lund et al., 2008; Schwertmann and Cornell, 2000). Ferrihydrite was synthesized using hydrothermal precipitation reported by Zhang (Zhang et al., 2007). Lepidocrocite was synthesized according to the previous reports (Lewis and Farmer, 1986; Li et al., 2022). Additionally, schwertmannite was prepared by H_2O_2-driven $FeSO_4 \cdot 7H_2O$ oxidation (Regenspurg et al., 2004). Magnetite was acquisited from Sinopharmatic Chemical Reagent Co., LTD. The detailed synthesis methods are provided in the Supplementary Material (Text S1).

2.2. Characterization

X-ray diffraction (XRD) was carried out using a Bruker D8 Advance diffractometer equipped with a Cu Kα radiation (λ = 0.15406 Å, 40 kV and 40 mA). The diffraction data were collected over an angular range $5° < 2\theta < 85°$ with a scanning rate of $10°$ min^{-1} and a step of $0.02°$. Scanning electron microscopy (SEM, S4800) and transmission electron microscopy (TEM, Talos F200X) were used to analyze the morphologies and structures of the six minerals. Additionally, selected area electron diffraction (SAED) and energy dispersive X-ray spectroscopy (EDS) were applied to observe mineral crystal structures and elemental distribution. The specific surface area and pore size distribution were measured by Brunauer–Emmett–Teller (BET) (Micromeritics 2460). X-ray photo-electron spectroscopy (XPS, Thermo Scientific K-Alpha) was used to investigate the properties of hydroxyl sites at an acceleration voltage of 12 kV and filament current of 6 mA. Fourier-transform infrared (FT-IR) spectra were recorded on a Bruker VERTEX70 FTIR spectrometer in the range 400–4000 cm^{-1} to identify the existing functional groups of iron (oxyhydr)oxides nanoparticles. The sample preparation for the FT-IR analysis followed by mixing 1 mg of iron (oxyhydr)oxides nano-particles with 100 mg KBr before the test. The data were preprocessed using Bruker OPUS software. XANES measurements at the As K-edge of iron (oxyhydr)oxide samples were performed at the 1W1B beam line of the Beijing Synchrotron Radiation Facility (BSRF, China). Positron annihilation lifetime spectroscopy (PAL) was carried out at University of Science and Technology of China (USTC) to reveal the micropore structure of six samples. The Detailed characterization are described in Text S2.

2.3. Batch experiments

Adsorption kinetic and isotherms experiments were conducted on a

thermostatic shaker with a velocity of 280 rpm at 25 °C. As_2O_3 and $Na_2HAsO_4 \cdot 7H_2O$ were used as arsenite and arsenate sources, respectively. The pH of the six iron-bearing mineral suspensions was adjusted to 6.0 using HCl (0.1 M) and NaOH (0.1 M). All experiments were carried out three times. The suspension was immediately filtered through a 0.22 μm membrane filter and the dissolved arsenic concentrations were quantified with an atomic fluorescence spectrometer (AFS-9700). The Details are described in Text S3.

Arsenic desorption experiments were carried with an ionic strength of 0.02 M $NaNO_3$, at initial As(III) and As(V) concentrations ranging from 1.06 μM to 13.35 μM. The suspensions were prepared at a concentration of 0.3 g L^{-1} and stirred on a magnetic mixer with a speed of 280 rpm for 24 h. The solution pH was adjusted to 6.0. After 24 h, the supernatant was passed through a 0.22 μm membrane filter. The filtered supernatant was collected to measure the concentrations of arsenic adsorbed on these iron (oxyhydr)oxides. After arsenic adsorption and desorption equilibrium was reached, 305 μmol L^{-1} Na_3PO_4 was added to the remaining solid phase in a 100 ml centrifuge tube, which was placed in a thermostatic shaker with a velocity of 280 rpm at 25 °C. After 24 h, the supernatant was collected to test the concentrations of As.

2.4. Nanofiltration membrane filtration experiment

Nanofiltration membrane analysis to determine molecular size of arsenite and arsenate (NF-2012-100G, desalination rate 90 %, size 298 mm × 47 mm; purchased from Guangdong JCBR Technology Co., LTD.) was performed at an operating pressure of 0.45 MPa (65 psig) using deoxygenated deionized water (pH 6.0). The molecular size analysis also performed to explore the effects of concentration on the separation of As (III) and As(V). The initial stock solution concentrations of As(III) and As (V) ranged from 0.13 to 13.35 μM. The pH was adjusted to 6.0 using HCl (0.1 M) and NaOH (0.1 M). Additionally, the effect of pH on the separation of As(III) and As(V) was studied. The initial As(III) and As(V)

stock solutions were prepared at a concentration of 2.0 μM and the pH was adjusted to 5.0, 6.0, 7.0 and 8.0, respectively. The same pair of membrane coupons was used for all the experiments. 2 L of the solution was passed through the nanofiltration membrane at a flow rate of 15.8 L h^{-1}. After filtering for 3 min, 10 ml of the filtrate was collected for analysis by an atomic fluorescence spectrometer (AFS-9700). After experiment, the nanofiltration membrane was washed using deoxygenated deionized water for at least 10 min to avoid nanofiltration membrane fouling and blocking. All the experiments were carried out at room temperature.

3. Results

3.1. Bulk characterization

Fig.S1 shows the X-ray diffraction (XRD) patterns of the synthesized hematite, magnetite, goethite, lepidocrocite, ferrihydrite, and schwertmannite minerals, which matched well with their corresponding references from the crystallographic database (JCPDS No. 33-0664; No. 19-0629; No. 29-0713; No. 08-0098; No. 29-0712; No. 47-1775) and no impurities could be observed. The strong intensity and large half peak width in the XRD patterns of hematite and magnetite revealed their well crystallinity. SEM and TEM images of the six iron (oxyhydr)oxides are shown in Fig.S2 and Fig. 1. SEM images revealed relatively uniform and spherical particles of hematite and magnetite (Fig. S2a and b). The lattice fringes in the hematite particles were 0.37, 0.27, and 0.22 nm (Fig. 1b), which were assigned to the (012), (104), and (113) facets, respectively, as evidenced by the selected-area electron diffraction (SAED) analysis (Fig. 1b). The magnetite nanoparticles, however, exhibited a distinctive hourglass-shaped loop (constriction in the central region), which can be attributed to the presence of different magnetic phases with varying coercivities or a combination of particle size distributions (Roberts et al., 1995; Roberts et al., 2000; Tauxe et al., 1996).
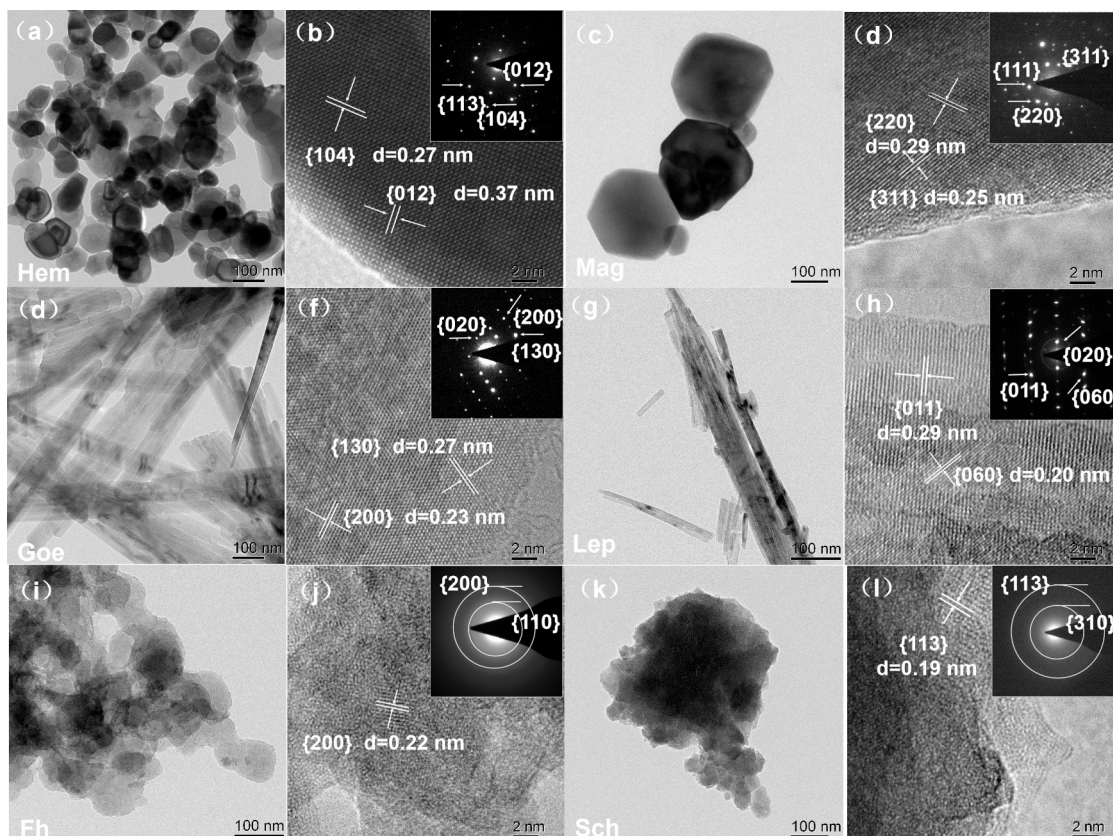

Fig. 1. TEM and SAED images in hematite (a), magnetite (b), goethite (c), lepidocrocite (d), ferrihydrite (e), and schwertmannite (f).

The lattice fringes of magnetite particles were 0.29 and 0.25 nm, which correspond to the (220) and (311) facets on the sides, respectively (Fig. 1c). Goethite exhibited a multi-domain structure along the needle axis (Fig. S1c) that showed an orderly arrangement on its crystal surface, which was consistent with previous literature (Kugbe et al., 2009). The measured lattice fringes of goethite were respectively 0.23 and 0.27 nm, corresponding to (200) and (130) facets (Fig. 1f). The lepidocrocite particles exhibited a rod-like morphology with exposed lattice fringes of 0.29 and 0.20 nm (Fig. S1d, and Fig. 2h), which were attributed to (011)

and (060) facets, respectively (Kader et al., 2015; Lewis and Farmer, 1986). In addition, SEM and TEM images of ferrihydrite and schwertmannite showed an irregular shape with many small particles aggregated (Fig. S2e-d and Fig. 1i, k), suggesting a poor crystallinity. The ferrihydrite particles showed a lattice fringe of 0.22 nm, which matched the interplanar spacing of the (200) facet (Fig. 1j), while that in schwertmannite was 0.19 nm, corresponding to the (113) facet. The specific surface areas of hematite, magnetite, goethite, lepidocrocite, ferrihydrite, and schwertmannite, obtained from Brunnauer-Emmett-
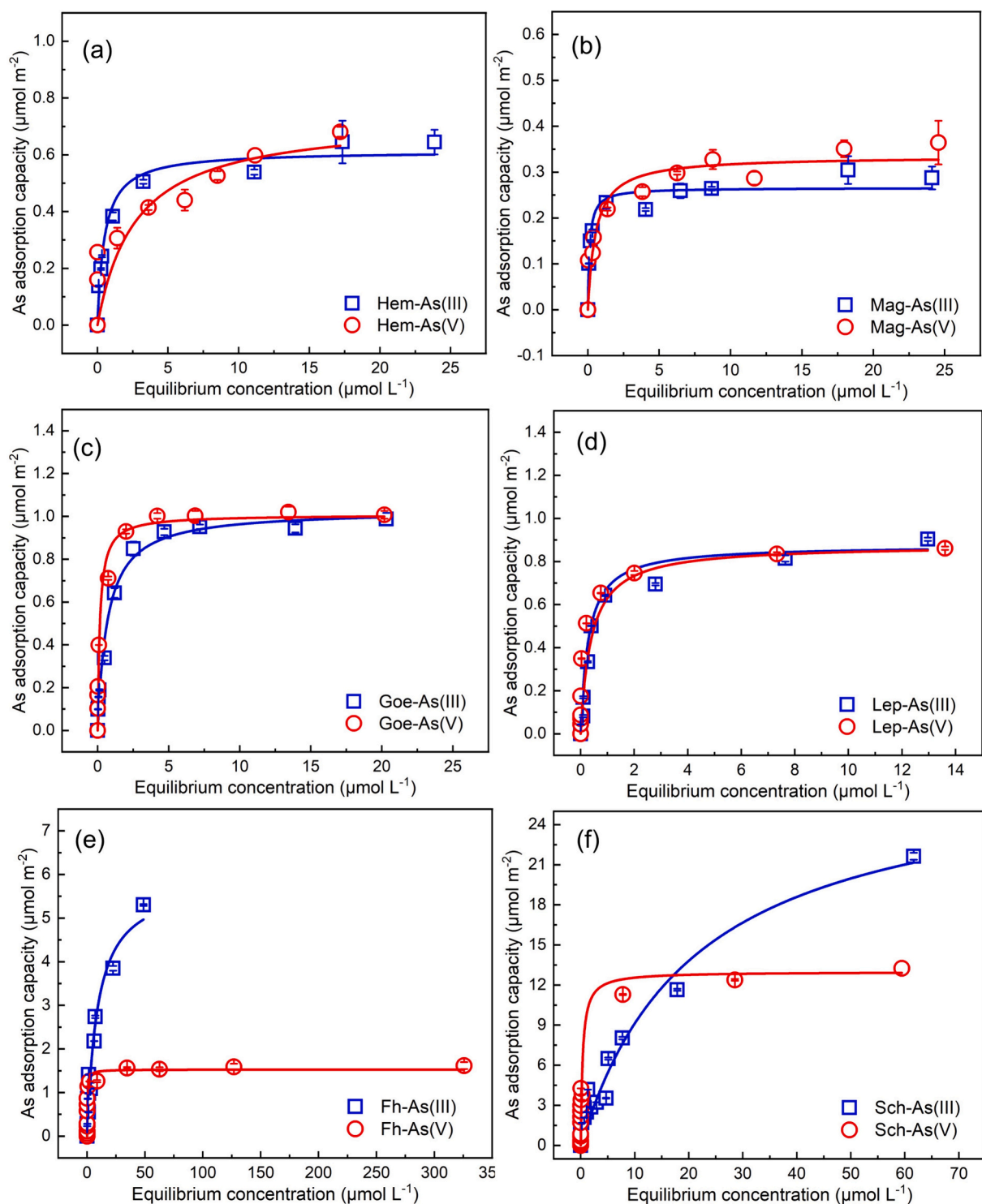

Fig. 2. Adsorption isotherms of As(III) and As(V) on (a) hematite, (b) magnetite, (c) goethite, (d) lepidocrocite, (e) ferrihydrite and (f) schwertmannite at pH 6.0. The datas were fitted using Langmuir models.

Teller (BET) model, were 27.7, 39.2, 43.1, 101.3, 308.0, and 104.4 m^2 g^{-1}, respectively.

3.2. Arsenic adsorption experiments

Fig. 2 displays the adsorption isotherms for As(III) and As(V). The results obtained from fitting the Langmuir and Freundlich models are presented in Fig. 2 and Table S1. Since the six iron (oxyhydr)oxides show different specific surface areas, their maximum adsorption amount per unit surface area were calculated for comparison purpose. As shown in Fig. 2, As(III) and As(V) adsorption were different for the six iron (oxyhydr)oxides. The maximum As(V) adsorption of hematite was 0.73 µmol m^{-2}, which was higher than that of As(III) (0.61 µmol m^{-2}) (Table S1). Magnetite showed a similar behavior as hematite, i.e., As(V) (0.33 µmol m^{-2}) was more favorably adsorbed by hematite compared to As(III) (0.27 µmol m^{-2}). Interestingly, we observed an opposite trend regarding As(V) and As(III) adsorption on ferrihydrite and schwertmannite, i.e., the maximum As(III) adsorption on ferrihydrite and schwertmannite was 5.77 and 28.41 times higher than those of As(V), respectively, indicating that As(III) species had a relatively high adsorption affinity in ferrihydrite and schwertmannite compared to As(V). In addition, the maximum adsorption amounts of As(III) and As(V) (1.03 vs 1.01 µmol m^{-2}) on goethite were very close to each other. This phenomenon was also observed in lepidocrocite for As(III) and As(V) (0.88 vs 0.88 µmol m^{-2}) adsorption.

3.3. Evolution of arsenic species on iron (oxyhydr)oxides

The phase structure and morphology can affect the reactivity of (oxyhydr)oxides because of their different exposed lattice facets with having different surface energies. Therefore, the phase structure and morphology of the iron (oxyhydr)oxides before and after adsorbing As(III) and As(V) were analyszed, as evidenced by XRD, SAED patterns, and HRTEM images (Fig. S4, S5, and Text S4). The results showed that the iron (oxyhydr)oxides after the adsorption with As(III) and As(V) also still showed the same phase structure and morphology, which were consistent with the previous reports (Ou et al., 2024). Furthermore, we analyzed the residual arsenic contents in the iron minerals after reaction with As(V) and As(III) using TEM-EDS mapping analysis (Fig. S3 and Table S2). The As/Fe molar ratios of hematite, magnetite, goethite, lepidocrocite, ferrihydrite, and schwertmannite after As(V) adsorption were 0.0029, 0.0025, 0.0073, 0.015, 0.25, and 0.37, respectively, while after As(III) adsorption, their corresponding As/Fe molar ratios changed to 0.0012, 0013, 0.0051, 0.016, 0.25, and 0.37, respectively. This result indicated that the immobilization capacities of As(III) and As(V) on different iron minerals had significant differences. It should be noted that EDS analysis is a semi-quantitative approach used to determine the residual arsenic content in iron minerals. To confirm the adsorption capacities of different iron minerals, this method must be combined with adsorption experiments. To determine whether the different behavior towards As(III) and As(V) adsorption on six iron minerals is attributed to the change of arsenic speciation, we employed As K-edge XANES spectra to analyze oxidation state of As adsorbed on iron (oxyhydr)oxides after reaction with As(III) and As(V). As shown in Fig. S6, two strong peaks at ~11,871.3 and ~11,874.0 eV were assigned to As(III) and As(V) species, respectively (Fang et al., 2023; Hong et al., 2023). After reaction with As(V), the As adsorbed energy on six minerals remained the same as in the Na$_2$HAsO$_4$ powder, indicating that As(V) species did not change after reaction with iron (oxyhydr)oxides. Previous literature reported that As(III) oxidation could take place on iron minerals (e.g., ferrihydrite and goethite) (Sun and Doner, 1998; Zhao et al., 2011). We found that the arsenic specie of As(III) adsorbed iron oxides are mainly in the form of As(III), but still exist little fraction of As(V) species. There are two reasons that may cause the As(III) oxidation. The first reason is the As(III) oxidation mediated by the iron (oxyhydr)oxides. Another one is the exposure of X-ray beam with great photon flux to samples, which has raised concerns from previous works (Canche-Tello et al., 2015; George et al., 2012). In this study, we further examined the As species of As adsorbed iron oxide samples using XPS analysis (Fig. S7), which have relatively low incident energy to the samples compared to synchrotron light sources. However, we did not observe the As(V) species in the As(III) adsorbed iron oxides. The results indicated that As(III) oxidation is likely to be caused by the exposure of X-ray beam. In addition, in order to further reveal the complex of As(III)/As(V) on iron (oxyhydr)oxides, we collected FTIR spectra of iron (oxyhydr)oxides before and after reacting with As(III)/As(V) (Fig.S8 and Text S5).

3.4. Pore distribution

The pore size distributions in iron (oxyhydr)oxides were analyzed through N$_2$ adsorption and desorption isotherms. As shown in Fig. 3, the pore size distributions in hematite and magnetite samples showed a relatively low adsorption volume of N$_2$ molecules at low pressures (P/P$_0$ < 0.01) indicating that there were very few micropores in hematite and magnetite samples (Fig. 3a-d). The pore size for hematite and magnetite mainly occurred at ~31.8 Å, which fell into the mesopore size range (2–50 nm) as defined by the International Union of Pure and Applied Chemistry (IUPAC). Goethite and lepidocrocite showed relatively high adsorption volume of N$_2$ molecules at low pressures (P/P$_0$ < 0.01) compared to hematite and magnetite. The calculated pore sizes were ~ 25.2 Å for goethite and ~ 27.3 Å for lepidocrocite, which belonged to the mesopore size. In addition, shoulder peaks at ~ 17.2 and 14.8 Å were also observed in goethite and lepidocrocite, respectively, suggesting that goethite and lepidocrocite not only contain mesopores, but also have a certain amount of micropores. Compared to these four iron (oxyhydr)oxides, the two minerals ferrihydrite, and schwertmannite showed a swift increase in N$_2$ adsorption at low pressures (P/P$_0$ < 0.01) (Fig. 3e-h), indicating that ferrihydrite and schwertmannite had a well-developed micropore structure (< 2 nm). The predominate pore sizes were ~ 5.0, ~ 13.6, and ~ 25.2 Å for ferrihydrite and ~ 14.2 and ~ 25.2 Å for schwertmannite.

Positron annihilation lifetime (PAL) spectrum exhibits a high level of sensitivity towards the porous and/or vacancy structure present in materials, which could be used for detecting the structure of micropores (Ling et al., 2022; Zhang et al., 2017; Zheng et al., 2015). Fig. 4 illustrates the peak-normalized PAL profiles of hematite, magnetite, goethite, lepidocrocite, ferrihydrite, and schwertmannite. The PAL spectrum could be decomposed into three distinct components based on previous reports using LTv9 program (Kong et al., 2011; Liao et al., 2023; Tang et al., 1999; Zheng et al., 2023). The shortest lifetime component (τ_1) of 174–206 ps was attributed to the free annihilation of positrons in defect-free crystal (Dutta et al., 2007; Kong et al., 2011). The medium lifetime component (τ_2) of 365.5–409.8 ps was assigned to the size of large vacancy clusters in minerals. The lifetime value of τ_2 could indicate the size of vacancy clusters, which is positively correlated with the vacancy clusters. Nagai et al. reported that the positron lifetime of 350–400 ps corresponded to the presence of vacancy clusters, measuring 10–20 atom in size, which are big enough to form vacancy cluster-like micropore structures on the iron (oxyhydr)oxides (Nagai et al.,2003). The longest lifetime component (τ_3) at 2.18–2.46 ns corresponded to the annihilation of orthopositronium atoms formed in the unoccupied space among minerals grains (Liu et al., 2009). Therefore, vacancy clusters and large voids contribute to the micropores in iron (oxyhydr)oxides. We found that the intensity of τ_3 (I_3) in the six mineral samples ranged from 0.5 % to 2.0 %, which was far lower than their corresponding intensity of τ_2 (I_2), indicating that vacancy clusters are the primary contribution to the formation of micropore structure in iron (oxyhydr)oxides. However, the I_2 in six samples has a significant difference, i.e., the I_2 value in ferrihydrite (83.5 %) and schwertmannite (86.8 %) was obviously larger than that in goethite (70.7 %) and lepidocrocite (59.1 %), followed by hematite (56.6 %) and magnetite (46.6 %).
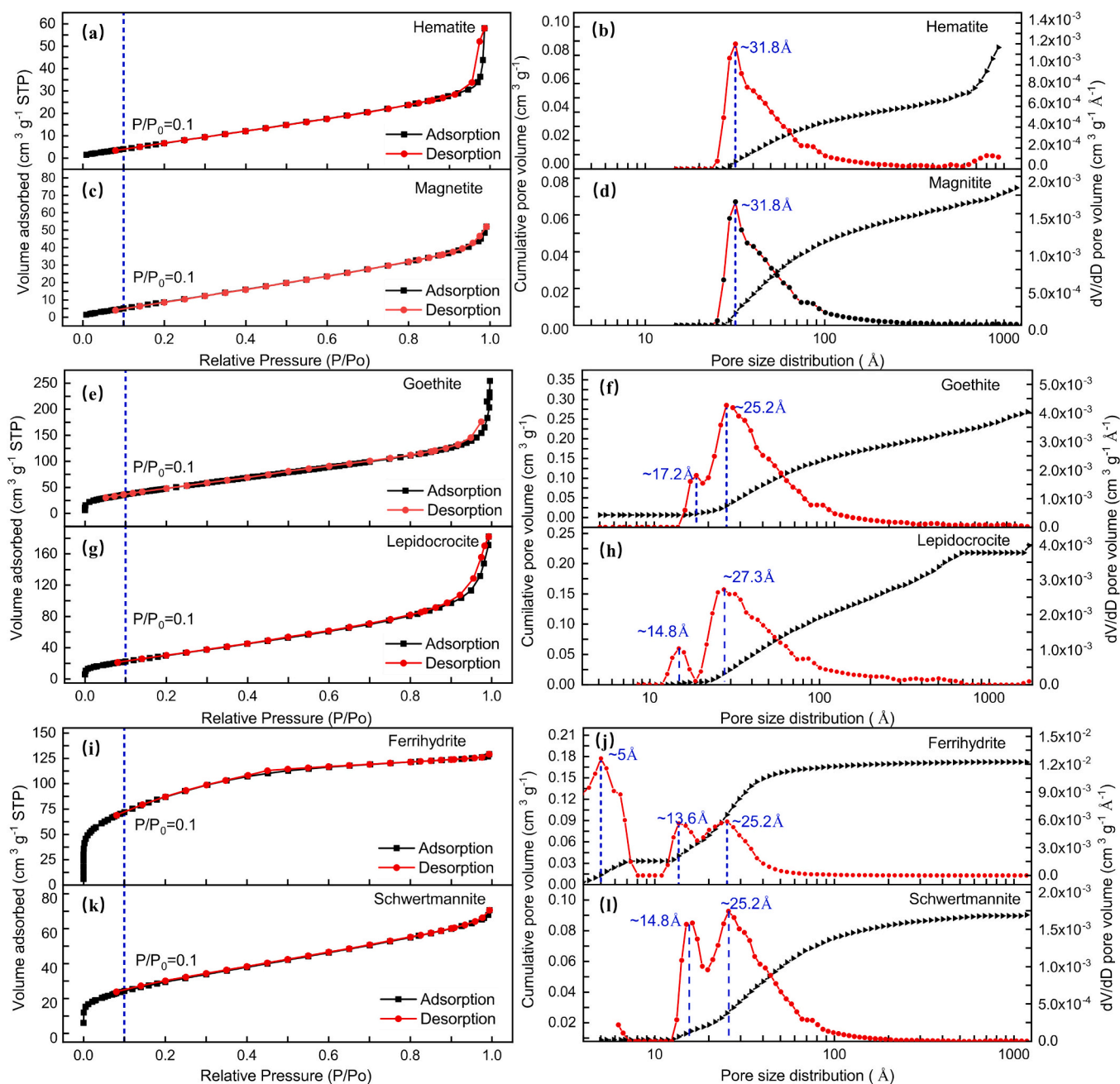
Fig. 3. N$_2$ adsorption and desorption isotherms, pore-size distribution and volume of hematite (a, b), magnetite (c, d), goethite (e, f), lepidocrocite (g, h), ferrihydrite (i, j), and schwertmannite (k, l). The datas were derived by the adsorption isotherms using the non-linear density functional theory (NLDFT) method.

3.5. The contributions of micropores sites to arsenic immobilization

Fig. 5 shows the arsenic adsorption amount on six typical iron minerals as a function of reaction time. The data for the corresponding kinetic were obtained using the intra-particle diffusion (IPD) model. The IPD model was described as follows (Tan and Hameed, 2017).

$$Q_t = k_p t^{0.5} + c$$

where the amount of arsenic adsorbed on iron (oxyhydr)oxides at a given time (h) was determined by Q_t, the IPD rate constant (μmol g^{-1} h$^{-1/2}$) was determined by k_p, and C (μmol g^{-1}) represented the thickness of the boundary layer.

Fig. 5 illustrates the plots of Q_t versus $t_{1/2}$ for As(V) and As(III) adsorption on six typical iron (oxyhydr)oxides, respectively. The fitted

parameters are showed in Table S3. According to previous reports, the complete adsorption composes of three steps (Ho et al., 2000; Tan and Hameed, 2017). The adsorption rate during the initial period (e.g., 0–2 h) is determined by the first step, which is the movement of the adsorptive from the aqueous phase to the exterior surface of the adsorbent (external diffusion). Because of the influence of pore diameters, the second step involves the diffusion of the adsorptive from the surface into the pore structure of the adsorbent (pore diffusion), which is much slower than the exterior diffusion. The third step, however, is very fast in comparison to the previous two steps, and attributes to the reaction between the adsorptive and internal surface sites of the sorbent. In this study, we observed that a straight line could fit well the plot for As(III) and As(V) adsorption on hematite and magnetite over the entire reaction using IPD model (Fig. 5a and b). Remarkably, the plots for As(III) and As (V) adsorption on other four iron (oxyhydr)oxides were not linear, but
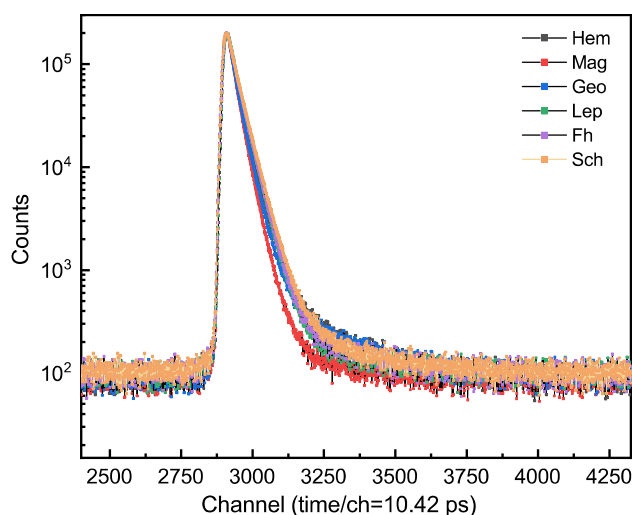
Fig. 4. Positron annihilation lifetime spectrum of magnetite, goethite, hematite, lepidocrocite, ferrihydrite, and schwertmannite.

could be assigned to two linear sections (Fig. 5c-f). The slope for As(V) on hematite (2.43) and magnetite (2.67) was obviously larger than their corresponding slops for As(III) (11.53 and 1.45), respectively (Table S3). For goethite and lepidocrocite, the slopes for As(III) and As(V) at second linear section (K_{p2}) became small compared to those at first linear section (K_{p1}), suggesting that pore diffusion rate (K_{p2}) influences the overall adsorption rate on goethite and lepidocrocite. Interestingly, the K_{p2} of As(III) (2.75 and 15.16) on goethite and lepidocrocite was higher than that of As(V) (1.83 and 13.97), respectively. In addition, the K_{p2} of As(III) for ferrihydrite and schwertmannite further increased to 139.6 and 80.2, while those for As(V) increased to 63.4 and 55.1, respectively. This result revealed that adsorption behaviors of As(III) and As(V) are different over iron minerals.

In principle, the desorption behavior of arsenic adsorbed on micropore sites should be different from that on surface sites, i.e., the desorption of arsenic adsorbed on micropore sites presents a greater challenge compared to the adsorption on the surface, which is primarily due to the restricted diffusion from the internal pore to the bulk aqueous phase. Therefore, the desorption behavior of arsenic adsorbed on iron minerals could reflect the involvement of micropore sites for the As(III) immobilization. Fig. 6 presents the desorbed arsenic amount against the adsorbed arsenic amount on different iron minerals. The slope reflects the mobility of arsenic adsorbed on iron minerals, and the larger the slope, the easier desorption of arsenic adsorbed. For hematite, the desorption behavior of As(V) adsorption could be divided into two sections (Fig. S10). At first section with relatively low initial arsenic concentration, the slope for As(V) (0.385) was close to that for As(III) (0.376). While the slope for As(V) (0.106) was lower than that for As(III) (0.385) at second section with higher initial arsenic concentration. The comprehensive slope for As(III) was larger than that for As(V) (0.154) (Fig. 6a). Magnetite showed the same trends as hematite, i.e., the comprehensive slope for As(III) was 2 times higher than that for As(V) (Fig. 6b). This result indicated that As(III) is more readily desorbed than As(V) from hematite and magnetite. Compared to hematite and magnetite, the slopes for As(III) in goethite (0.184) and lepidocrocite (0.244) were close to their corresponding slopes for As(V) (0.159 and 0.283), respectively. While the slopes for As(III) in ferrihydrite (0.021) and schwertmannite (0.071), however, were obviously much lower than those for As(V) (0.057 and 0.203), respectively, indicating that the As(III) desorption varied in comparison to As(V) on different iron (oxyhydr)oxides. Moreover, we observed that the slopes for As(III) in ferrihydrite and schwertmannite were lower than those in goethite and lepidocrocite, followed by hematite and magnetite. The relatively low slopes for As(III) mean that the desorption of As(III) in ferrihydrite and

schwertmannite became difficult compared to the other four iron (oxyhydr)oxdies. It is evident from this observation that micropore sites play a crucial role in the adsorption of As(III) on iron (oxyhydr)oxides, leading to distinct differences in the adsorption behaviors of As(III) and As(V) on iron minerals.

4. Discussion

4.1. As(III) versus As(V) adsorption on iron minerals

Iron minerals have a strong affinity to arsenic species in As polluted groundwaters (Deng et al., 2019; Fang et al., 2021; Lan et al., 2018; Mertens et al., 2016; Zhang et al., 2018). We evaluated the arsenic adsorption capacities of six (oxyhydr)oxides under the same experimental condition to observe possible differences for As(III) and As(V) immobilization (Fig. 2). In this study, we observed that As adsorption behavior on iron minerals can be divided into three scenarios. The first scenario, i.e. a relatively high As(V) adsorption compared to As(III) happened on hematite and magnetite. The second scenario is relevant for goethite and lepidocrocite, which showed very similar adsorption amount of both As(V) and As(III). The third scenario, i.e. higher As(III) adsorption than As(V), occurred in ferrihydrite and schwertmannite. The results of TEM-EDS mapping analysis also confirmed the batch adsorption experiments. The As/Fe molar ratios of hematite and magnetite after As(V) adsorption (0.0029 and 0.0025) were clearly greater than those after As(III) adsorption (0.0012 and 0.0013). On the contrary, the As/Fe molar ratios of ferrihydrite and schwertmannite after As(V) adsorption (0.095 and 0.21) were far lower than those after As(III) adsorption (0.25 and 0.37). In addition, the As/Fe molar ratios of goethite and lepidocrocite after As(III) adsorption (0.0051 and 0.016) were similar to those after As(V) adsorption (0.0073 and 0.015). The specific surface areas had obvious differences among six iron minerals, which influenced the total arsenic adsorption amount of iron minerals. However, we had normalized the As adsorption amount of minerals divided by their corresponding specific surface areas (Fig. 2). Therefore, the specific surface areas could be used to explain the difference in As adsorption amount among iron minerals (e.g., ferrihydrite and schwertmannite with high specific surface areas show larger adsorption amount of As(III) and As(V) than hematite and magnetite with relatively small specific surface areas), but were not responsible for the significant adsorption differences between As(III) and As(V) on the same minerals.

Remarkably, we found that there was a seesaw effect influencing the As(III) vs As(V) adsorption on iron minerals, which was plausibly controlled by the degree of crystallinity, i.e., poorly-crystalline iron minerals (e.g., ferrihydrite and schwertmannite) showed higher As(III) adsorption, while well poorly-crystalline iron minerals (e.g., hematite and magnetite) are better for As(V) immobilization. Correspondingly, the similar adsorption capacity of As(V) to As(III) occurred in the iron minerals with having the degree of crystallinity between poor and well (e.g., goethite and lepidocrocite). This result suggested that the significant adsorption difference between As(III) and As(V) on different minerals is not random, but has strong regularity. However, it seems to be hasty that attributed the significant adsorption differences between As(III) and As(V) on different minerals to their crystallinity degrees. This is because that the degree of crystallinity reflects the macroscopic phenomenon of mineral structure confirmed by XRD patterns, which cannot provide the detailed differences of microstructure behind it, such as pore size distribution. In addition, the interaction between arsenic and minerals may also change the phase structure and morphology of minerals, chemical species of arsenic adsorbed on minerals, and the arsenic immobilization manners (e.g., surface precipitation and structural doping). These possible influence factors still need to be further discussed in details.
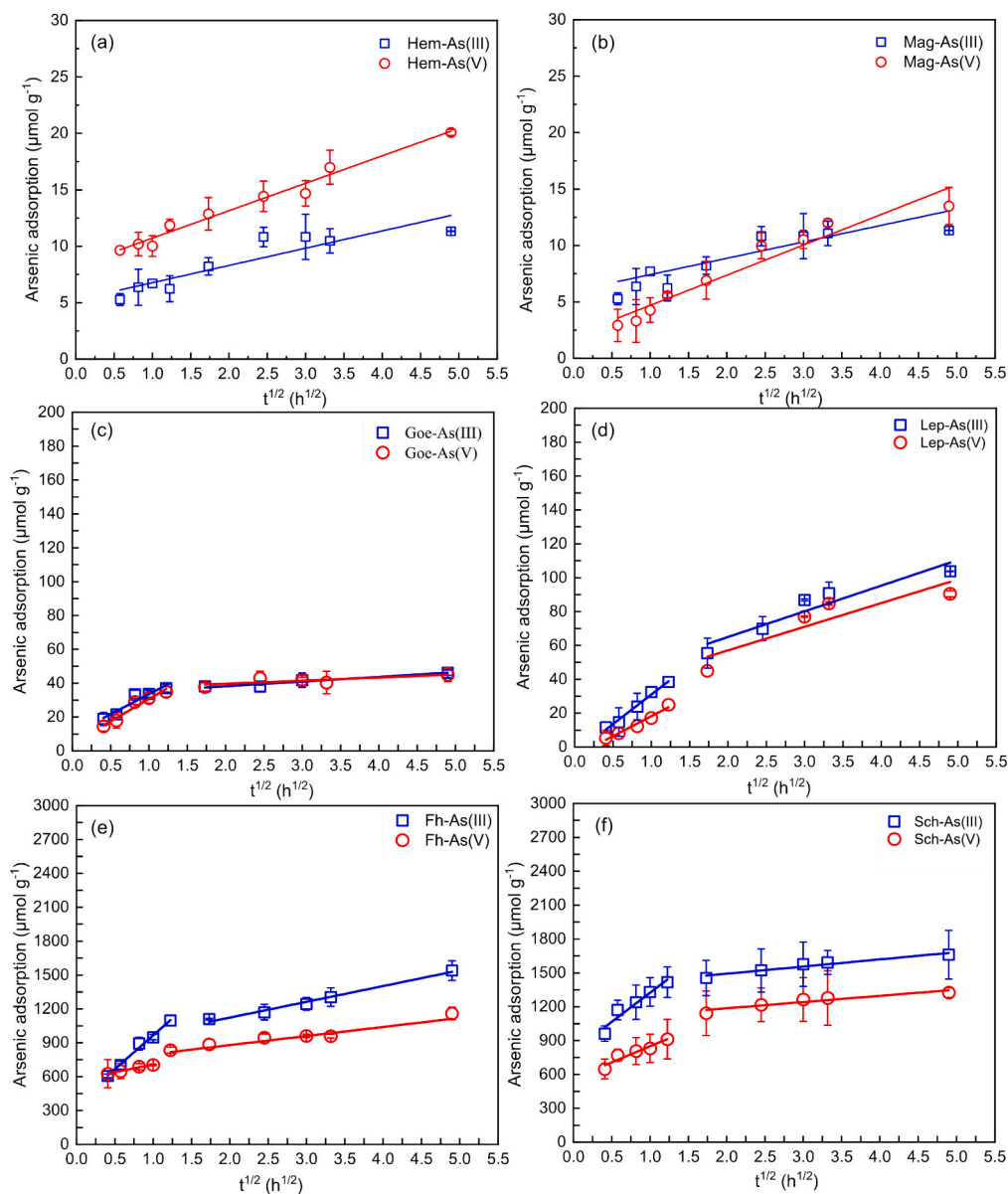
Fig. 5. Intraparticle diffusion model for arsenic adsorption on six typical iron (oxyhydr)oxides.

4.2. The impact of phase structure, morphology, and arsenic species iron (oxyhydr)oxides

From the arsenic adsorption experiments, the main resulting question is why there is high As(V) immobilization compared to As(III) in well-crystalline iron (oxyhydr)oxides, while sorption is opposite on poorly-crystalline iron (oxyhydr)oxides and more or less equal for As(III) and As(V) on relatively poor-crystalline (oxyhydr)oxides. Previous studies have observed that the phase structure of iron minerals might affect arsenic adsorption (Shi et al., 2021; Wang et al., 2016). We therefore examined the phase transformation of iron (oxyhydr)oxides after the As(III) and As(V) adsorption. In this study, we initially ruled out the possible transformation of phase for hematite, magnetite, goethite, and lepidocrocite after the As(III) and As(V) adsorption, because these four iron minerals had relatively stable structure compared to ferrihydrite and schwertmannite (Fig. S1). However, we still did not observe the phase transformation of ferrihydrite and schwertmannite, which was confirmed by the XRD analysis and their corresponding SAED patterns (Fig. S4 and S5) and HRTEM images (Fig. S5). Previous studies had observed the transformation of poorly-crystalline minerals (e.g.,

ferrihydrite) to well-crystalline iron minerals, but this process taken place in extremely low transformation rates at pH 2–7 in pure mineral suspensions, i.e., 2.0×10^{-5}-7.5×10^{-5} h^{-1} (Das et al., 2011a). In addition, in an As-iron mineral suspension system, co-existing arsenic species were observed to retard the transformation of poorly-crystalline (oxyhydr)oxide (Das et al., 2011), thereby further decreasing the transformation rate. In this study, we set the parameters of reaction pH and temperature for all batch adsorption experiments as 6.0 and 25 °C, respectively. Under this condition, the phase transformation of schwertmannite and ferrihydrite was too gradual to be observed. The results indicated that changes of phase structure and morphology can be ruled out and therefore are not responsible for the different adsorption behavior of As(III) and As(V) to the six different iron minerals.

The arsenic species has been shown to significantly influence the migration and fate of As in natural environments. The traditional view is that As(V) is an oxyanion with a negative charge at an wide pH range of 4–9, exhibiting a high affinity to iron (oxyhydr)oxides (Marinho et al., 2019). In contract, As(III) is a neutral oxyanion (e.g., H_3AsO_3) at neutral pH that shows weak binding to iron minerals (Jia et al., 2023; van Genuchten et al., 2023). The XANES, As3d XPS revealed that arsenic
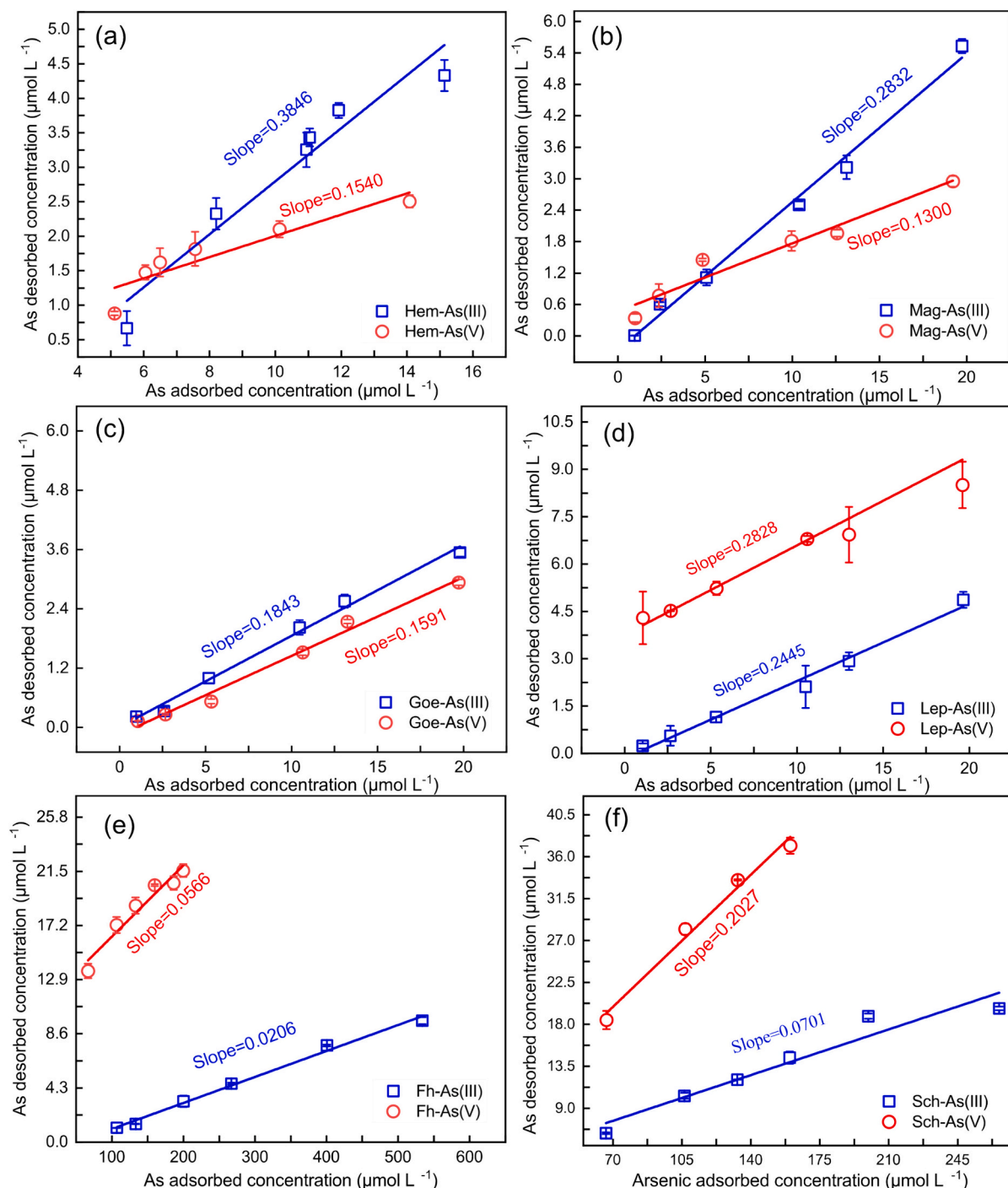
Fig. 6. The concentration of arsenic desorption versus arsenic adsorption at pH = 6.0.

speciess adsorbed on iron (oxyhydr)oxides did not undergo oxidation or reduction. Previous studies showed that As(III) oxidation on iron (oxy-hydr)oxides require high initial Fe/As ratios. For example, Zhao et al. confirmed that As(III) oxidation on poorly-crystalline ferrihydrite occurred at high Fe/As ratio (e.g., 50 and 200) within a short time (e.g., 1 day), while As(III) oxidation did not occur at a relatively low initial Fe/As ratio (e.g., 5) (Zhao et al., 2011). In our study, the initial Fe/As ratio employed for As(III) adsorption on poorly-crystalline ferrihydrite and schwertmannite was not higher than 10, because these ratios showed better adsorption capacities for As(III) adsorption. In addition to the required Fe/As ratio, also the reaction time needs to be long enough. For example, the relatively well-crystalline goethite was observed to oxidize

As(III) to As(V) at acidic pH, but it took a long time (20 days) with a low As(III) oxidation rate (20 % within this time frame) (Sun and Doner, 1998). Since the reaction time in our batch adsorption experiments was 24 h, it was too short to observe As(III) oxidation by iron minerals such as hematite, magnetite, lepidocrocite, and goethite.

4.3. Effect of surface precipitation and structural incorporation

Adsorption is mainly responsible for As(III) and As(V) immobiliza-tion on iron minerals. However, other processes such as structural incorporation and surface-precipitation of arsenic species were also observed to affect arsenic immobility under certain conditions. For

instance, Bolanz et al. observed that As(V) could dope into the structure of well-crystalline hematite under high temperature (200 °C) and long aging time (e.g., 7 days) with high initial $As_2O_5/Fe(NO_3)_3$ reactant molar ratio (0.5) (Bolanz et al., 2013). From our adsorption experiments, the experiments were conducted at 25 °C for 1 d, and also the initial As/Fe molar ratio for arsenic adsorption experiments was lower than 0.5. Therefore, We excluded structural incorporation of As(III) or As(V) into the six iron minerals. However, the incorporation of arsenic species into the structure of some iron (oxyhydr)oxides such as schwertmannite through exchange process should not be completely ignored. This is because schwertmannite contains structural sulfate groups (SO_4^{2-}), which could be exchanged by As(V) and As(III), thereby promoting binding of As(III) and As(V) by schwertmannite (Adra et al., 2013; Burton et al., 2009). Nevertheless, this still cannot reasonably explain why As(III) is adsorbed more readily than As(V) by schwertmannite. In addition to structural incorporation, surface precipitation could also increase the total arsenic adsorption on iron minerals, although this process was typically observed to take place under more rigorous conditions such as low pH and high As/Fe ratio. Jia et al. found surface precipitation at acidic pH of 3–5 in an arsenate-ferrihydrite system (Jia et al., 2006). Tokoro et al. further demonstrated that ferric arsenate via surface-precipitation would be formed at pH 5 and 7 when the initial molar ratio As/Fe was higher than 0.4, otherwise, As(V) mainly adsorbed on ferrihydrite via surface complexation (Tokoro et al., 2010). Notably, in our experiments the As/Fe molar ratio in schwertmannite after reaction with As(III) (0.37), determined by EDS-mapping, was the highest one among all the samples after reaction with As(III) and As(V), which was still slightly lower than 0.4. Moreover, the relative high pH value (e.g., 6.0) used for our adsorption experiments was probably preventing the formation of surface precipitates. These two main reasons explain why we did not detect any new mineral phases such as ferric arsenate after the reaction of the iron (oxyhydr)oxides with arsenic.

4.4. Effect the micropore structure and size of arsenic ions

The chemical binding analysis of As species on the surface of iron (oxyhydr)oxides has been widely investigated using XAS and density function theory (DFT) calculations in previous work (Dzade et al., 2014; Hattori et al., 2009; Kiejna and Pabisiak, 2012). For example, we have studied the adsorption behaviors of As(III) and As(V) species on octahedral and tetrahedral sites of iron mineral using DFT calculations in our previous work (Zheng et al., 2023), According to previous work, iron minerals mainly consist of octahedral and tetrahedral Fe—O units (R. M. Cornell Schwertmann, 2003). This result indicated that the chemical bonding of As(V) on iron minerals surface was thermodynamically favorable compared to that of As(III). This observation could be used to exclude surface adsorption sites for promoting As(III) immobilization.

In general, there are two types of adsorption sites available for arsenic immobilization by iron (oxyhydr)oxides. The first type is surface sites where ions and/or molecules can be directly immobilized independent of their size. The second type is binding sites in pores of the minerals, where the size of the ions and/or molecules matches well can enter. In this study, we not only observed the micropores (< 2 nm) in the iron minerals, but also detected the mesopore (2–5 nm) and macropore (larger than 50 nm). The peak at ~ 31.8 Å in the hematite and magnetite indicated that they had much more mesopores (Fig. 3b and d), and no peaks attributed to micropores were observed. The recurrence of ~ 25.2 Å in goethite, ferrihydrite, and schwertmannite indicated that they have the similar mesopore size. Although micropore and mesopore sizes occurred simultaneously in the goethite and lepidocrocite, the fraction of micropore numbers was obviously lower than that of mesopore. In addition, the intensity of peaks in ferrihydrite and schwertmannite, attributed to the micropores, became strong, indicating that an obvious increase in the number of micropores for these two iron minerals. Apparently, the ratio of micropores to mesopores in ferrihydrite and

schwertmannite was higher than that in goethite and lepidocrocite. This result indicated that ferrihydrite had abundance of micropore sites compared to goethite and lepidocrocite available for arsenic immobilization.

Moreover, we employed PAL spectra to reveal that the micropores did not primarily originate from unoccupied space among minerals grains because of their relatively low I_3 values (Table 1). Correspondingly, we observed the strong signals of τ_2 (I_2) in minreals that was attributed to the vacancy-clusters consisting of 10–20 atoms deficiencies in iron minerals, indicating that vacancy clusters were the primary contribution to the formation of micropore structure in iron (oxyhydr) oxides. In our previous works, we confirmed that low-crystalline minerals with rough surface commonly had abundant vacancy defects (e.g., Iron and oxygen vacancies) (Hou et al., 2014; Hou et al., 2022; Liu et al., 2023; Xiang et al., 2024). Therefore, the poor crystallinity of iron minerals (e.g., ferrihydrite) was responsible for the high I_2 value. The largest I_2 value in ferrihydrite and schwertmannite revealed that they possessed the highest content of vacancy cluster-like micropores, which was in agreement with the fitting result of N_2 adsorption and desorption curves.

Interestingly, we found the micropore size of 5 Å in the ferrihydrite (Fig. 3j), which was slightly larger than a single iron octahedron. In general, this small size micropore is rarely to be identified in minerals. However, we could explain this observation using the result of PAL analysis. Considering that ferrihyrite had an abundance of atom deficiencies to form vacancy clusters, 5 Å was therefore one of the predominate size of vacancy clusters that existed in the ferrihydrite surface. In addition, it should be noted that the τ_2 component also appeared in well-crystalline hematite and magnetite samples, suggesting that they also had some microporous structure. These results also suggested that the PAL technique was more sensitive than the traditional N_2 adsorption isotherms for micropore characterization.

It need to consider that the size of arsenic ions should be match well with micropore size of iron minerals, otherwise, the micropore sites were not adequately utilized by the arsenic ions. In general, H_3AsO_3 and $H_2AsO_4^-$ are the main As(III) and As(V) species at pH 6.0, respectively. The hydrated ionic radius of H_3AsO_3 and $H_2AsO_4^-$ calculated based on Stokes-Einstein equation were 4.22 and 5.90 Å (Takahashi et al., 2011), respectively. The relatively small size of As(III) compared to As(V) indicated that it has a high probability to enter the small micropore sites in iron (oxyhydr)oxides. To further illustrate the effect of ionic size on the immobilization of arsenic species, we performed the nanofiltration (NF) membrane filtration (< 2 nm) experiments to calculate the rejection rate of As(III) and As(V) under the same condition. As shown in Fig. S9, although the initial As concentration and pH affected the rejection by NF membrane, the rejection rate of As(III) by the NF membrane was always lower than that of As(V) at any given initial As concentration and pH, suggesting that As(III) species had relatively small size compared to As(V) species, which agreed well with the calculation result based on Stokes-Einstein equation. The relatively small size of As(III) species meant that it was easier to pass through the small pores (e.g., < 2 nm) than As(V), which had high probability to enter the micropore sites of iron minerals.

Table 1
Position lifetime parameters of magnetite, goethite, hematite, lepidocrocite, ferrihydrite, and schwertmannite.

Samples	τ_1(ps)	τ_2 (ps)	τ_3 (ns)	I_1 (%)	I_2 (%)	I_3 (%)
Hematite	174.1	410.9	2.227	41.38	56.61	2.01
Magnetite	206.5	365.5	2.391	53.08	46.43	0.50
Goethite	187.5	373.8	2.460	39.04	59.10	1.86
Lepidocrocite	192.9	375.9	2.590	28.56	70.74	0.70
Ferrihydrite	175.7	386.0	2.307	12.53	86.52	0.95
Schwertmannite	182.4	409.8	2.181	15.05	83.84	1.11

4.5. The underlying contribution of the micropore sites

We revealed a seesaw effect observed in different iron minerals for As(III) and As(V) immobilization that originated from the size of oxyanion arsenic species as well as the occurrence of vacancy-cluster like micropore sites. This could be further described as follows. Hematite and magnetite had well crystallinities with very few vacancy cluster-like micropores, As(III) and As(V) mainly utilized surface sites for immobilization. Therefore, the relatively larger affinity of As(V) in iron minerals compared to As(III) resulted in a higher As(V) adsorption. For the goethite and lepidocrocite, they possessed some vacancy cluster-like micropores, which could be readily used by As(III) and counteracted the adverse effect of its low affinity in iron minerals, thereby showing the similar adsorption towards to As(III) and As(V). While ferrihydrite and schwertmannite had an abundance of micropores, which provided additional adsorption sites for promoting immobilization of As(III) due to its relatively small size compared to As(V), leading to a higher As(III) immobilization. In this study, we successfully employed the IPD model to illustrate the underlying contribution of the micropore sites that involve in As(III) immobilization. In general, the IPD model considers three step adsorption processes, which can be used to distinguish the rate-limiting steps during the entire reaction. The third step is very fast in comparison to the previous two steps (external diffusion and pore diffusion), which means that the third step does not control the rate for adsorption throughout its entirety. The plot for As(III) and As(V) adsorption on hematite and magnetite was well fitted by using only one straight line. This result suggested that external diffusion, rather than pore diffusion, was the predominate process influencing the As(III) and As(V) immobilization on hematite and magnetite due to their few micropores. The larger slope for As(V) compared to As(III) on hematite and magnetite further demonstrated that As(V) was more readily immobilized than As(III), which was in agreement with isothermal adsorption results. Remarkably, we used two linear sections to well fit the As(III) and As(V) adsorption kinetics on goethite, lepidocrocite, ferrihydrite, and lepidocrocite through IPD model. This observation indicated that the overall adsorption was impacted by two rate-limiting processes of external and pore diffusions. For goethite and lepidocrocite, the slopes for As(III) and As(V) at second linear section (K_{p2}) became small compared to those at first linear section (K_{p1}), suggesting that pore diffusion rate influences the overall adsorption rate due to the existence of some micropores. We still observed the relatively higher K_{p2} of As(III) compared to As(V) for both goethite and lepidocrocite, suggesting that the effect of pore diffusion on As(III) adsorption was smaller than that on As(V), which could be explained by the relatively low size of As(III)

compared to As(V). The further increased K_{p2} of As(III) and As(V) on ferrihydrite and schwertmannite compared to goethite and lepidocrocite indicated that the effect extent of pore diffusion for As(III) and As(V) adsorption became strong, which was attributed to their abundant micropore sites that participated in the As(III) and A(V) immobilization. Similarly, the higher K_{p2} of As(III) compared to As(V) was also observed in ferrihydrite and schwertmannite, indicating that the smaller-sized oxyanion As(III) can effectively utilize the micropore sites for adsorption, resulting in high As(III) adsorption on ferrihydrite and schwertmannite.

To sum up, micropore sites play vital roles in affecting the fate of arsenic, leading to a seesaw effect for As(III) and As(V) immobilization on iron minerals. The presence of micropore sites promoted As(III) and As(V) immobilization, while their contribution to the degree of improvement for As(III) immobilization are obviously larger than that for As(V). This was attributed to the relatively small size of As(III) compared to that of As(V), which matched well with the size of vacancy-cluster like micropore sites. Fig. 7 presents a schematic diagram showcasing the disparity in adsorption between As(III) and As(V) caused by pore sites in iron (oxyhydr)oxides. It should be noted that mesopores and macropores also existed in iron (oxyhydr)oxides, the size of oxyanions As(III) and As(V), however, is far smaller than that of mesopore (2–50 nm) and macropore (> 50 nm) size. Therefore, the mesopores and macropores could directly participate in the As(III) and As(V), but were not the main factor contributing to the varying adsorption capacities of iron minerals towards As(III) and As(V).

4.6. Environmental and geological implications

Iron-bearing minerals are found in virtually all terrestrial and aquatic environments controlling arsenic mobility. The crystallinity and phase structure of environmental iron (oxyhydr)oxides are significantly affected by the conditions such as redox conditions, temperature, and hydration status of the environmental habitat, leading to different mineral reactivities towards sorption of As(III) and As(V). Relatively low As(III) adsorption capacities on iron (oxyhydr)oxides compared to that of As(V) were widely accepted in the past. The findings of this study provide novel insights into the vacancy cluster-like micropore sites in minerals that act as active "hotspot" affecting the fate of pollutants, which aids to precisely developing strategies for understanding and controlling arsenic pollution. For example, in environment with alternating redox dynamics (e.g., paddy soils), the reductive dissolution of iron (oxyhydr)oxides as well as the change of arsenic speciation from As(V) to As(III) are usually regarded as the two major factors leading to a
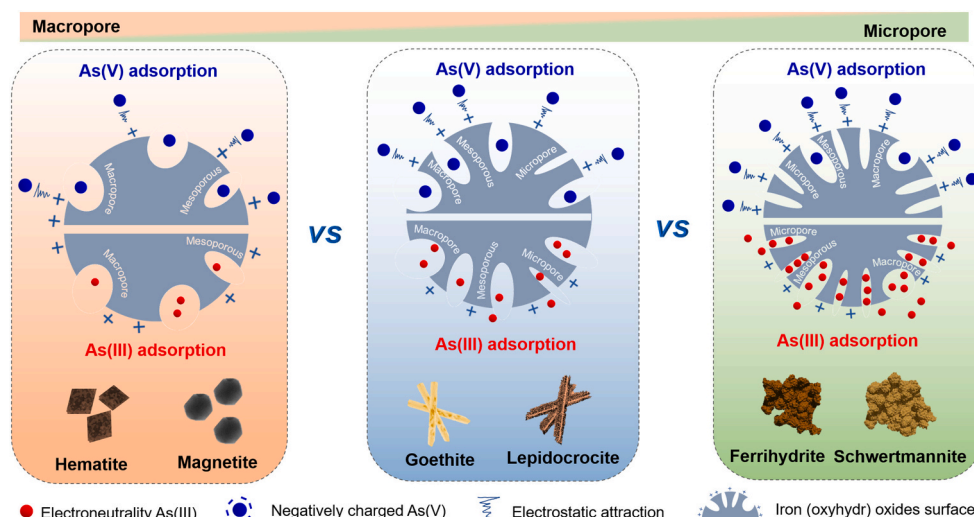

Fig. 7. Schematic diagram of the role of micropore sites in As(III) and As(V) immobilization on six typical iron minerals.

significant increase in arsenic mobility(Xu et al., 2017). Following our results, a strategy of controlling the degree of dissolution of iron (oxyhydr)oxides through water management for generating metastable iron minerals with abundant vacancy cluster-like micropore sites seems to be more promising than a strategy of transforming As(III) to As(V) for arsenic immobilization.

5. Conclusions

In this work, the arsenic adsorption on iron minerals for As(III) and As(V) were employed to carefully examine the significantly difference of adsorption capacity on iron (oxyhydr) oxides in environment with different forms arsenic. The analysis result of TEM-EDS mapping, FTIR spectra, N_2 adsorption/desorption curves, and X-ray absorption spectroscopy revealed that the adsorption capacities of As(III) and As(V) on six typical iron (oxyhydr)oxides confirmed the existence of two other As (III)/As(V) adsorption scenarios with sorption of As(V) ≈ As(III) and As (V) < As(III), in addition to As(V) > As(III) observed in previous work. For the first time, we provided PAL evidence to reveal that vacancy cluster-like micropores, consisting of 10–20 atom deficiencies, are intrinsic properties and widely distributed in iron minerals. We found that the content of vacancy cluster-like micropores in ferrihydrite and schwertmannite was larger than that in goethite and magnetite, followed by lepidocrocite and hematite. In addition, the relatively small hydrated ionic radius of the oxyanion As(III) compared to the larger As (V) species enabled the As(III) to easily enter the micropores, which provided additional adsorption sites for As immobilization. The findings of this study provide novel insights into a seesaw effect for As(III) and As (V) immobilization on iron mineral controlled by the vacancy cluster-like micropore sites.

CRediT authorship contribution statement

Juan Liu: Writing – original draft, Methodology, Investigation, Formal analysis. **Yixin Duan:** Formal analysis. **Hao Chen:** Software, Formal analysis. **Bangjiao Ye:** Supervision, Software. **Hongjun Zhang:** Supervision, Software, Formal analysis. **Wenfeng Tan:** Supervision. **Andreas Kappler:** Writing – review & editing, Supervision. **Jingtao Hou:** Writing – review & editing, Visualization, Supervision, Software, Conceptualization.

Declaration of competing interest

The authors declare that they have no known competing financial interests or personal relationships that could have appeared to influence the work reported in this paper.

Data availability

Data will be made available on request.

Acknowledgments

Appendix A. Supplementary data

Supplementary data to this article can be found online at https://doi.org/10.1016/j.scitotenv.2024.176376.

References

Adra, A., Morin, G., Ona-Nguema, G., Menguy, N., Maillot, F., Casiot, C., Bruneel, O., Lebrun, S., Juillot, F., Brest, J., 2013. Arsenic scavenging by aluminum-substituted ferrihydrites in a circumneutral pH river impacted by acid mine drainage. Environ. Sci. Technol. 47, 12784–12792. https://doi.org/10.1021/es4020234.

Bolanz, R.M., Wierzbicka-Wieczorek, M., Čaplovičová, M., Uhlík, P., Göttlicher, J., Steininger, R., Majzlan, J., 2013. Structural incorporation of As⁵⁺ into hematite. Environ. Sci. Technol. 47, 9140–9147. https://doi.org/10.1021/es305182c.

Bujňáková, Z., Baláž, P., Zorkovská, A., Sayagués, M.J., Kováč, J., Timko, M., 2013. Arsenic sorption by nanocrystalline magnetite: an example of environmentally promising interface with geosphere. J. Hazard. Mater. 262, 1204–1212. https://doi.org/10.1016/j.jhazmat.2013.03.007.

Burton, E.D., Bush, R.T., Johnston, S.G., Watling, K.M., Hocking, R.K., Sullivan, L.A., Parker, G.K., 2009. Sorption of arsenic(V) and arsenic(III) to schwertmannite. Environ. Sci. Technol. 43, 9202–9207. https://doi.org/10.1021/es902461x.

Canche-Tello, J., Vargas, M.C., Hérnandez-Cobos, J., Ortega-Blake, I., Leclercq, A., Solari, P.L., Lezama-Pacheco, J., Den Auwer, C., Mustre de Leon, J., 2015. X-ray accelerated photo-oxidation of As(III) in solution. J. Phys. Chem. A 119, 2829–2833. https://doi.org/10.1021/jp510596p.

Cornell Schwertmann, R.M., 2003. The Iron Oxides: Structure, Properties, Reactions, Occurences and Uses, The Iron Oxides.

Das, S., Hendry, M.J., Essilfie-Dughan, J., 2011. Effects of adsorbed arsenate on the rate of transformation of 2-Line ferrihydrite at pH 10. Environ. Sci. Technol. 45, 5557–5563. https://doi.org/10.1021/es200107m.

Deng, Y.X., Weng, L.P., Li, Y.T., Ma, J., Chen, Y.L., 2019. Understanding major NOM properties controlling its interactions with phosphorus and arsenic at goethite-water interface. Water Res. 157, 372–380. https://doi.org/10.1016/j.watres.2019.03.077.

Dutta, S., Chattopadhyay, S., Sutradhar, M., Sarkar, A., Chakrabarti, M., Sanyal, D., Jana, D., 2007. Defects and the optical absorption in nanocrystalline ZnO. J. Phys. Condens. Matter 19, 236218. https://doi.org/10.1088/0953-8984/19/23/236218.

Dzade, N.Y., Roldan, A. De, Leeuw, N.H., 2014. A density functional theory study of the adsorption of benzene on hematite (α-Fe₂O₃) surfaces. Minerals 4, 89–115. https://doi.org/10.3390/min4010089.

Fang, Z.Y., Li, Z.X., Zhang, X.L., Pan, S.Y., Wu, M.F., Pan, B.C., 2021. Enhanced arsenite removal from silicate-containing water by using redox polymer-based Fe(III) oxides nanocomposite. Water Res. 189, 116673. https://doi.org/10.1016/j.watres.2020.116673.

Fang, L., Hong, Z., Borch, T., Shi, Q., Li, F., 2023. Iron vacancy accelerates Fe (II)-induced anoxic As(III) oxidation coupled to iron reduction. Environ. Sci. Technol. 57, 2178–2185. https://doi.org/10.1021/acs.est.2c07833.

van Genuchten, C.M., Hamaekers, H., Fraiquin, D., Hollanders, S., Ahmad, A., 2023. Heavy metal removal potential of olivine. Water Res. 245, 120583. https://doi.org/10.1016/j.watres.2023.120583.

George, G.N., Pickering, I.J., Pushie, M.J., Nienaber, K., Hackett, M.J., Ascone, I., Hedman, B., Hodgson, K.O., Aitken, J.B., Levina, A., Glover, C., Lay, P.A., 2012. X-ray-induced photo-chemistry and X-ray absorption spectroscopy of biological samples. J. Synchrotron Radiat. 19, 875–886. https://doi.org/10.1107/s090904951203943x.

Giménez, J., Martínez, M., de Pablo, J., Rovira, M., Duro, L., 2007. Arsenic sorption onto natural hematite, magnetite, and goethite. J. Hazard. Mater. 141, 575–580. https://doi.org/10.1016/j.jhazmat.2006.07.020.

Hattori, T., Saito, T., Ishida, K., Scheinost, A.C., Tsuneda, T., Nagasaki, S., Tanaka, S., 2009. The structure of monomeric and dimeric uranyl adsorption complexes on gibbsite: a combined DFT and EXAFS study. Geochim. Cosmochim. Acta 73, 5975–5988. https://doi.org/10.1016/j.gca.2009.07.004.

Ho, Y.S., Ng, J.C.Y., McKay, G., 2000. Kinetics of pollutant sorption by biosorbents: review. Sep. Purif. Methods 29, 189–232. https://doi.org/10.1081/SPM-100100009.

Hong, Z., Li, F., Borch, T., Shi, Q., Fang, L., 2023. Incorporation of cu into goethite stimulates oxygen activation by surface-bound Fe(II) for enhanced As(III) oxidative transformation. Environ. Sci. Technol. 57, 2162–2174. https://doi.org/10.1021/acs.est.2c07065.

Hou, J., Li, Y., Mao, M., Ren, L., Zhao, X., 2014. Tremendous effect of the morphology of birnessite-type manganese oxide nanostructures on catalytic activity. ACS Appl. Mater. Interfaces 6, 14981–14987. https://doi.org/10.1021/am5027743.

Hou, J.T., Tan, X.K., Xiang, Y.J., Zheng, Q., Chen, C., Sha, Z.J., Ren, L., Wang, M.X., Tan, W.F., 2022. Insights into the underlying effect of Fe vacancy defects on the adsorption affinity of goethite for arsenic immobilization. Environ. Pollut. 314, 120268. https://doi.org/10.1016/j.envpol.2022.120268.

Jia, Y., Xu, L., Fang, Z., Demopoulos, G.P., 2006. Observation of surface precipitation of arsenate on ferrihydrite. Environ. Sci. Technol. 40, 3248–3253. https://doi.org/10.1021/es051872+.

Jia, Q.Q., Zhang, X.J., Deng, J., Huang, L.Z., 2023. Labile Fe(III) phase mediates the electron transfer from Fe(II,III) (oxyhydr) oxides to carbon tetrachloride. Water Res. 245. https://doi.org/10.1016/j.watres.2023.120636.

Jubb, A.M., Eskelsen, J.R., Yin, X., Zheng, J., Philben, M.J., Pierce, E.M., Graham, D.E., Wullschleger, S.D., Gu, B., 2018. Characterization of iron oxide nanoparticle films at the air-water interface in Arctic tundra waters. Sci. Total Environ. 633, 1460–1468. https://doi.org/10.1016/j.scitotenv.2018.03.332.

Kader, M.A., Moslehuddin, A.Z.M., Kamal, A.M., Mori, Y., 2015. Mineralogical composition of some selected paddy soils of Bangladesh. J. Fac. Agr. Kyushu U. 60, 463–470.

Kiejna, A., Pabisiak, T., 2012. Surface properties of clean and au or Pd covered hematite (α-Fe₂O₃) (0001). J. Phys. Condens. Matter 24, 095003. https://doi.org/10.1088/0953-8984/24/9/095003.

Kim, S.A., Guerinot, M.L., 2007. Mining iron: Iron uptake and transport in plants. FEBS Lett. 581, 2273–2280. https://doi.org/10.1016/j.febslet.2007.04.043.

Kong, M., Li, Y., Chen, X., Tian, T., Fang, P., Zheng, F., Zhao, X., 2011. Tuning the relative concentration ratio of bulk defects to surface defects in TiO_2 nanocrystals leads to high photocatalytic efficiency. J. Am. Chem. Soc. 133, 16414–16417. https://doi.org/10.1021/ja207826q.

Kugbe, J., Matsue, N., Henmi, T., 2009. Synthesis of Linde type A zeolite-goethite nanocomposite as an adsorbent for cationic and anionic pollutants. J. Hazard. Mater. 164, 929–935. https://doi.org/10.1016/j.jhazmat.2008.08.080.

Lan, S., Ying, H., Wang, X.M., Liu, F., Tan, W.F., Huang, Q.Y., Zhang, J., Feng, X.H., 2018. Efficient catalytic As(III) oxidation on the surface of ferrihydrite in the presence of aqueous Mn(II). Water Res. 128, 92–101. https://doi.org/10.1016/j.watres.2017.10.045.

Lewis, D., Farmer, V.J.C.M., 1986. Infrared absorption of surface hydroxyl groups and lattice vibrations in lepidocrocite (γ-FeOOH) and boehmite (γ-AlOOH). Clay Miner. 21, 93–100. https://doi.org/10.1180/claymin.1986.021.1.08.

Li, X., Guo, C., Jin, X., Yao, Q., Liu, Q., Zhang, L., Lu, G., Reinfelder, J.R., Huang, W., Dang, Z.J.E.S.N., 2022. Molecular-scale study of Cr (VI) adsorption onto lepidocrocite facets by EXAFS, in situ ATR-FTIR, theoretical frequency calculations and DFT+ U techniques. Environ. Sci. Nano 9, 568–581. https://doi.org/10.1039/D1EN01085A.

Liao, S., Su, L.L., Wan, Y.P., Yan, S.Y., Tang, X., Cheng, G.D., 2023. Calculations of positron annihilation lifetime in solid based on finite difference and conjugate-gradient methods. Nucl. Instrum. Methods Phys. Res., Sect. B 537, 71–76. https://doi.org/10.1016/j.nimb.2023.01.011.

Ling, L.L., Jiao, L., Liu, X.S., Dong, Y., Yang, W., Zhang, H.J., Ye, B.J., Chen, J., Jiang, H.L., 2022. Potassium-assisted fabrication of intrinsic defects in porous carbons for electrocatalytic CO_2 reduction. Adv. Mater. 34, 2205933. https://doi.org/10.1002/adma.202205933.

Liu, J., Xiang, Y., Chen, Y., Zhang, H., Ye, B., Ren, L., Tan, W., Kappler, A., Hou, J., 2023. Quantitative contribution of oxygen vacancy defects to arsenate immobilization on hematite. Environ. Sci. Technol. 33, 12453–12464. https://doi.org/10.1021/acs.est.3c03441.

Liu, X.W., Zhou, K.B., Wang, L., Wang, B.Y., Li, Y.D., 2009. Oxygen vacancy clusters promoting reducibility and activity of ceria nanorods. J. Am. Chem. Soc. 131, 3140–3141. https://doi.org/10.1021/ja808433d.

Liu, Q., Chen, Z., Tang, J., Luo, J., Huang, F., Wang, P., Xiao, R., 2021. Cd and Pb immobilisation with iron oxide/lignin composite and the bacterial community response in soil. Sci. Total Environ. 802, 149922. https://doi.org/10.1016/j.scitotenv.2021.149922.

Lund, T.J., Koretsky, C.M., Landry, C.J., Schaller, M.S., Das, S., 2008. Surface complexation modeling of Cu(II) adsorption on mixtures of hydrous ferric oxide and kaolinite. Geochem. T. 9, 9. https://doi.org/10.1186/1467-4866-9-9.

Mandal, B.K., Suzuki, K.T., 2002. Arsenic round the world: a review. Talanta 58, 201–235. https://doi.org/10.1016/S0039-9140(02)00268-0.

Marinho, B.A., Cristóvão, R.O., Boaventura, R.A.R., Vilar, V.J.P., 2019. As(III) and Cr(VI) oxyanion removal from water by advanced oxidation/reduction processes:a review. Environ. Sci. Pollut. Res. 26, 2203–2227. https://doi.org/10.1007/s11356-018-3595-5.

Mertens, J., Rose, J., Wehrli, B., Furrer, G., 2016. Arsenate uptake by Al nanoclusters and other Al-based sorbents during water treatment. Water Res. 88, 844–851. https://doi.org/10.1016/j.watres.2015.11.018.

Ni, Z., Zhang, C., Ma, H.A., Liu, J.B., Wang, Z.Q., Zhu, K.C., Li, M., Jia, H.Z., 2022. Facet-dependent photo-degradation of nitro polycyclic aromatic hydrocarbons on hematite under visible light: participation of environmentally persistent free radicals and reactive oxygen/nitrogen species. Appl. Catal. B-Environ. 318, 121816. https://doi.org/10.1016/j.apcatb.2022.121816.

Ou, Y., Chi, J., Li, F., Chen, Q., Fang, L., 2024. Unravelling molecular fractionation of dissolved organic matter on ferrihydrite-phosphate complexes. Chem. Geol. 645, 121887. https://doi.org/10.1016/j.chemgeo.2023.121887.

Pang, S.C., Chin, S.F., Anderson, M.A., 2007. Redox equilibria of iron oxides in aqueous-based magnetite dispersions: effect of pH and redox potential. J. Colloid Interface Sci. 311, 94–101. https://doi.org/10.1016/j.jcis.2007.02.058.

Qi, P., Pichler, T., 2014. Closer look at As(III) and As(V) adsorption onto ferrihydrite under competitive conditions. Langmuir 30, 11110–11116. https://doi.org/10.1021/la502740w.

Raven, K.P., Jain, A., Loeppert, R.H., 1998. Arsenite and arsenate adsorption on ferrihydrite: kinetics, equilibrium, and adsorption envelopes. Environ. Sci. Technol. 32, 344–349. https://doi.org/10.1021/es970421p.

Regenspurg, S., Brand, A., Peiffer, S., 2004. Formation and stability of schwertmannite in acidic mining lakes. Geochim. Cosmochim. Acta 68, 1185–1197. https://doi.org/10.1016/j.gca.2003.07.015.

Roberts, A.P., Cui, Y., Verosub, K.L., 1995. Wasp-waisted hysteresis loops: mineral magnetic characteristics and discrimination of components in mixed magnetic systems. J. Geophys. Res. 100, 17909–17924. https://doi.org/10.1029/95JB00672.

Roberts, A.P., Pike, C.R., Verosub, K.L., 2000. First-order reversal curve diagrams: a new tool for characterizing the magnetic properties of natural samples. J. Geophys. Res. Solid Earth 105, 28461–28475. https://doi.org/10.1029/2000JB900326.

Schwertmann, U., Cornell, R.M., 2000. Iron Oxides in the Laboratory: Preparation and Characterization. John Wiley & Sons. https://doi.org/10.1002/9783527613229.

Shi, M., Min, X., Ke, Y., Lin, Z., Yang, Z., Wang, S., Peng, N., Yan, X., Luo, S., Wu, J., Wei, Y., 2021. Recent progress in understanding the mechanism of heavy metals retention by iron (oxyhydr)oxides. Sci. Total Environ. 752, 141930. https://doi.org/10.1016/j.scitotenv.2020.141930.

Sun, X., Doner, H.E., 1998. Adsorption and oxidation of arsenite on goethite. Soil Sci. 163.

Takahashi, Y., Sakamitsu, M., Tanaka, M., 2011. Diffusion coefficients of arsenate and arsenite in water at various pH. Chem. Lett. 40, 1187–1188. https://doi.org/10.1246/cl.2011.1187.

Tan, K.L., Hameed, B.H., 2017. Insight into the adsorption kinetics models for the removal of contaminants from aqueous solutions. J. Taiwan Inst. Chem. Eng. 74, 25–48. https://doi.org/10.1016/j.jtice.2017.01.024.

Tang, Z., Hasegawa, M., Shimamura, T., Nagai, Y., Chiba, T., Kawazoe, Y., Takenaka, M., Kuramoto, E., Iwata, T., 1999. Stable vacancy clusters in neutron-irradiated graphite: evidence for aggregations with a magic number. Phys. Rev. Lett. 82, 2532–2535. https://doi.org/10.1103/PhysRevLett.82.2532.

Tauxe, L., Mullender, T.A.T., Pick, T., 1996. Potbellies wasp-waists and superparamagnetism in magnetic. J. Geophys. Res. Solid Earth 101, 571–583. https://doi.org/10.1029/95JB03041.

Tokoro, C., Yatsugi, Y., Koga, H., Owada, S., 2010. Sorption mechanisms of arsenate during coprecipitation with ferrihydrite in aqueous solution. Environ. Sci. Technol. 44, 638–643. https://doi.org/10.1021/es902284c.

Wang, X.M., Zhu, M.Q., Koopal, L.K., Li, W., Xu, W.Q., Liu, F., Zhang, J., Liu, Q.S., Feng, X.H., Sparks, D.L., 2016. Effects of crystallite size on the structure and magnetism of ferrihydrite. Environ. Sci.-Nano. 3, 190–202. https://doi.org/10.1039/c5en00191a.

Wang, I., Gao, Y., Wang, X., Cai, R., Chung, C., Iftikhar, S., Wang, W., Li, F., 2021. Liquid metal shell as an effective iron oxide modifier for redox-based hydrogen production at intermediate temperatures. ACS Catal. 11, 10228–10238. https://doi.org/10.1021/acscatal.1c02102.

Xiang, Y., Liu, J., Chen, Y., Zhang, H., Ren, L., Ye, B., Tan, W., Kappler, A., Hou, J., 2024. The change of coordination environments induced by vacancy defects in hematite leads to a contrasting difference between cation Pb (II) and oxyanion As (V) immobilization. Environ. Pollut. 344, 123318. https://doi.org/10.1016/j.envpol.2024.123318.

Xu, X., Chen, C., Wang, P., Kretzschmar, R., Zhao, F., 2017. Control of arsenic mobilization in paddy soils by manganese and iron oxides. Environ. Pollut. 231, 37–47. https://doi.org/10.1016/j.envpol.2017.07.084.

Zhang, G., Qu, J., Liu, H., Liu, R., Wu, R., 2007. Preparation and evaluation of a novel Fe–Mn binary oxide adsorbent for effective arsenite removal. Water Res. 41, 1921–1928. https://doi.org/10.1016/j.watres.2007.02.009.

Zhang, G., Liu, H., Qu, J., Jefferson, W., 2012. Arsenate uptake and arsenite simultaneous sorption and oxidation by Fe–Mn binary oxides: influence of Mn/Fe ratio, pH, Ca^{2+}, and humic acid. J. Colloid Interface Sci. 366, 141–146. https://doi.org/10.1016/j.jcis.2011.09.058.

Zhang, G., Liu, F., Liu, H., Qu, J., Liu, R., 2014. Respective role of Fe and Mn oxide contents for arsenic sorption in iron and manganese binary oxide: an X-ray absorption spectroscopy investigation. Environ. Sci. Technol. 48, 10316–10322. https://doi.org/10.1021/es501527c.

Zhang, H.J., Sellaiyan, S., Kakizaki, T., Uedono, A., Taniguchi, Y., Hayashi, K., 2017. Effect of free-volume holes on dynamic mechanical properties of epoxy resins for carbon-fiber-reinforced polymers. Macromolecules 50, 3933–3942. https://doi.org/10.1021/acs.macromol.7b00472.

Zhang, W., Zhang, G.S., Liu, C.H., Li, J., Zheng, T., Ma, J., Wang, L., Jiang, J., Zhai, X.D., 2018. Enhanced removal of arsenite and arsenate by a multifunctional Fe-Ti-Mn composite oxide: Photooxidation, oxidation and adsorption. Water Res. 147, 264–275. https://doi.org/10.1016/j.watres.2018.10.001.

Zhao, Z., Jia, Y., Xu, L., Zhao, S., 2011. Adsorption and heterogeneous oxidation of As (III) on ferrihydrite. Water Res. 45, 6496–6504. https://doi.org/10.1016/j.watres.2011.09.051.

Zheng, J., Ji, G.B., Zhang, P., Cao, X.Z., Wang, B.Y., Yu, L.H., Xu, Z.C., 2015. Facile aluminum reduction synthesis of blue TiO_2 with oxygen deficiency for lithium-ion batteries. Chem. Eur. J. 21, 18309–18315. https://doi.org/10.1002/chem.201503266.

Zheng, Q., Hou, J., Hartley, W., Ren, L., Wang, M., Tu, S., Tan, W., 2020. As(III) adsorption on Fe-Mn binary oxides: are Fe and Mn oxides synergistic or antagonistic for arsenic removal? Chem. Eng. J. 389, 124470. https://doi.org/10.1016/j.cej.2020.124470.

Zheng, Q., Tu, S., Chen, Y., Zhang, H., Hartley, W., Ye, B., Ren, L., Xiong, J., Tan, W., Kappler, A., Hou, J., 2023. Micropore sites in ferrihydrite are responsible for its higher affinity towards As(III) relative to As(V). Geochim. Cosmochim. Acta 348, 27–40. https://doi.org/10.1016/j.gca.2023.03.007.